Proceedings of the 21st ICSMGE, Vienna, Austria, 14 – 19 June 2026. Pistrol, Adam & Schweiger (eds.)
Published by: ÖGG, Austrian Society for Geomechanics, Salzburg, Austria, ISBN 978-3-9503898-4-5
https://doi.org/10.53243/ICSMGE2026-1094

Deciphering the Dynamics of Immersed Granular Collapses via Seismic Signals: Implications for Submarine Geophysical Flows

Meichen Liu, Clarence Choi
Department of Civil Engineering, The University of Hong Kong, HKSAR, China, mchenliu@connect.hku.hk

ABSTRACT: This study investigates the dynamic behavior and seismic response of submarine granular column collapses through controlled laboratory experiments. By systematically varying the initial aspect ratio of the granular columns, we link the runout distance, basal effective stress, pore pressure with the measured seismic signals. Interpretation of experimental results shows that: (1) tall columns (i.e., high aspect ratios) generate long runout distances, strong basal stresses, and energetic seismic emissions, with seismic signals exhibiting increasing mean frequency and duration as aspect ratio increases; (2) dimensional analysis reveals that submarine granular flows are mainly controlled by frictional and viscous stresses, consistent with field observations; (3) a linear relationship is observed between the normalized runout distance and the densimetric Froude number *Fr*. This observation implies that *Fr* can serve as a reliable predictor of flow mobility, regardless of initial granular mass geometry; and (4) only a small fraction of the mechanical energy is converted into detectable seismic energy, with seismic efficiency reduced by intensified fluid–particle dissipation. These findings offer new insights into the coupling mechanisms between granular flow dynamics and seismic wave generation in submerged environments, with implications for submarine landslides monitoring and geohazard assessment.

KEYWORDS: Submarine granular collapse; seismic signal; aspect ratio; runout dynamics; energy dissipation; laboratory experiments.

1 INTRODUCTION

Submarine geophysical flows are natural mass movement processes that transport large volumes of sediments downslope under the cloak of the sea (Hampton et al., 1996; Du et al., 2023). These flows not only reshape submarine geomorphology but may generate geohazards, including the triggering of tsunamis and the destruction of seafloor infrastructure such as telecommunication cables and offshore pipelines (Walder et al., 2003). Therefore, understanding the dynamics of submarine granular flows, along with effective monitoring strategies, is essential for predicting their behavior and mitigating their associated hazards.

Compared to terrestrial settings, submarine flows are far more challenging to monitor directly using conventional methods. Globally, only around a dozen sites have successfully recorded small-scale (distance <50 km) submarine flow events using instruments installed within the flow path, such as moorings and embedded sensors. These devices frequently suffer damage or loss due to the intense sediment-laden currents and the difficulties posed by deployment in remote, deep-water locations (Paull et al., 2018). Observations of larger scale submarine flows remain extremely rare, with key velocity data mainly derived from indirect indicators (Talling et al., 2022). In recent years, passive seismic monitoring has revolutionized the understanding of terrestrial geohazards by remotely sensing ground motions in real time with millisecond temporal resolution and at relatively low cost (Cook et al., 2022). The seismic measurements hold even greater potential for advancing the understanding of submarine flows dynamics, given the various technological and environmental challenges of directly observing submarine processes (Clare et al., 2024; Kunath et al., 2025; Talling et al., 2023).

Submarine flows generate distinct seismic signatures through basal friction, particle collisions, and fluid-sediment interactions, which propagate through the seabed and water column (Clare et al., 2024; Kunath et al., 2025). However, existing seismic models—largely derived from terrestrial frameworks for bedload transport (Tsai et al., 2012), turbulent flow (Gimbert et al., 2014) and debris flows (Farin et al., 2019b)—fail to account for submarine-specific factors such as fluid-induced energy damping, transient pore-pressure changes in hyperconcentrated sediment layers governed by inelastic collision physics (Zhang et al., 2021), the momentum transfer dynamics of surge leading edges (Kunath et al., 2025), and non-monotonically frequency-dependent attenuation of Scholte waves at the seawater-seabed interface (Duncan et al., 2013). Interpreting the results from such models requires a detailed understanding of the coupling between submarine geophysical flow dynamics and the resulting seismic signals.

Despite advances of geophysical flows in field observations, experimental and numerical modeling (Arran et al., 2024; Baker et al., 2024; Clare et al., 2024; Kunath et al., 2025; Ng et al.,2013; Ng et al., 2017; Jiang et al., 2022; Yang et al., 2020; Polanía et al., 2024; Su & Choi, 2019), fundamental knowledge gaps remain in deciphering how initial geometries governs the submarine flow behavior (e.g., runout scaling, surge front dynamics, basal stress and pore pressure evolution, and energy conversion) and resultant seismic signatures.

In this study, we conduct a series of laboratory-scale submarine granular collapse experiments, systematically changing the initial aspect ratio to explore its effect on flow dynamics and the associated seismic emissions. Using high-speed imaging, pore pressure sensors, force transducers, and accelerometers, we capture the entire evolution of flow kinematics, basal stresses, pore pressure, and seismic signals. Particular attention is paid to interpreting the generated seismic energy and energy dissipation of the granular material.

2 METHODS

2.1 *Experimental Setup*

Figure 1 shows a side view of the newly developed experimental setup for this study. We conducted column collapse experiments in a rectangular channel that was 1000 mm long, 450 mm high, and 150 mm wide, under immersed conditions. The walls of the channel are made of acrylic boards. The retention and release of the granular material is controlled by a pneumatic gate to ensure repeatability. The gate lifts vertically at a velocity of 1.4 $m \cdot s^{-1}$. A wave absorber was also installed along the opposite end of the tank to minimize disturbances caused by reflected water waves. For the immersed experiments, water (i.e., density (ρ_w) of 1000 $kg \cdot m^{-3}$ and a dynamic viscosity (μ_f) of 0.001 Pa·s) was filled to a height of 400 mm. The granular columns were prepared with an initial length (L_0) of 100 mm and initial heights (H_0) from 100 to 350 mm, corresponding to aspect ratios ($A = H_0/L_0$) modelled were from 1 to 3.5. A summary of the modelled cases is given in Table 1. Glass beads with a density ρ_s of 2500 $kg \cdot m^{-}$

[3] were used for the granular mass. A single particle size (d_p = 3 mm) was tested. The ratio between the channel width and particle diameter W/d_p (with W = 15 cm being the channel width) was designed to be sufficiently large to ensure that side-wall effects did not influence the results (Jop & Pouliquen, 2005). Based on the flow regime classification proposed by Courrech du Pont et al. (2003), the generated granular mass flows can be characterized in the inertial regime, with a Stokes number ($St = \frac{1}{18\sqrt{2}} \frac{\sqrt{\rho_s(\rho_s-\rho_w)g d_p^3}}{\mu_f}$) of 39.17 and a density ratio ($r = \sqrt{\rho_s/\rho_w}$) of 1.58. It should be noted that although natural marine sediments are often cohesive and may contain clay minerals and organic matter, glass beads were used as a simplified analogue to isolate key physical processes and ensure experimental reproducibility. The results mainly apply to non-cohesive or weakly cohesive submarine granular flows, and extension to cohesive sediments is left for future work.

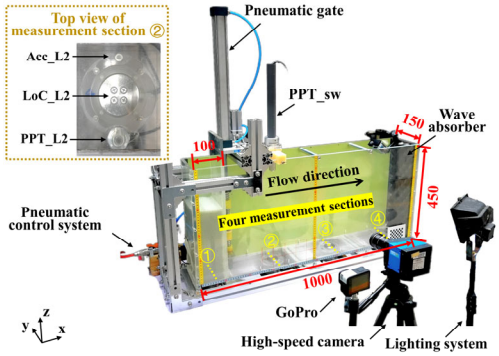

Figure 1. Experimental setup (all dimensions are in mm).

Table 1. Test program.

Test ID	d_p (mm)	A	ϕ_i	H_f (mm)	L_f (mm)	ϕ_{ft}
H10d3	3	1.0	0.6	74.60	345	0.472
H15d3		1.5		81.50	455	0.492
H20d3		2.0		91.00	550	0.483
H25d3		2.5		97.00	640	0.481
H30d3		3.0		106.0	720	0.485
H35d3		3.5		107.5	790	0.481

2.2 *Instrumentation*

A tri-axial load cell (LoC_L0) and a pore pressure transducer (PPT_L0) were installed directly beneath the initial column. At normalized runout distances (see Eq. 1) of approximately 2, 5, and 8 (x = 33, 61, 89 cm), each cross-section was equipped with a tri-axial load cell (LoC_L2, LoC_L5, LoC_L8), a pore pressure transducer (PPT_L2, PPT_L5, PPT_L8), and a vertical accelerometer (Acc_L2, Acc_L5, Acc_L8). An additional transducer (PPT_sw) above PPT_L2 measured surface waves (see Figure 1) for wave-effect correction (Du et al., 2023). Load cells recorded normal and shear stresses at 50 kHz, pore pressure transducers at 500 Hz, and accelerometers at 50 kHz with a 1k–25 kHz frequency response. Flow kinematics were captured by a high-speed camera (500 fps, 1312×1256 pixels), with PIV (Particle Image Velocimetry) analysis yielding velocity fields every 2 ms.

2.3 *Data Processing*

2.3.1 *Kinematic and Energetic Parameters*

To interpret the evolution of the submarine granular collapse, we compute kinematic (i.e., normalized runout distance $\tilde{L}$, front velocity U, and the center positions of granular mass) and energetic parameters (i.e., potential energy, kinetic energy, and the total energy loss) based on the time-resolved surface profile of the granular column obtained by high-speed camera. Figure 2(a) shows the extracted height field (z direction) H (x, t), where x is the horizontal coordinate along the base of the tank, and t denotes time. The flow is assumed to be quasi-two-dimensional, with negligible changes in the out-of-plane (y) direction. The temporal evolution of the normalized runout distance $\tilde{L}$ is:

$$\tilde{L} = (L - L_0)/L_0 \tag{1}$$

where L is the distance between the granular front and the left wall (x = 0). The front velocity U is computed as the average velocity between the times at which the front reaches 25% and 75% of the total runout distance, denoted as L_{25}=L_0+0.25(L_f−L_0) and L_{75}=L_0+0.75(L_f−L_0), respectively. To track the bulk motion of the granular mass, we compute the horizontal and vertical positions of the center of mass (COM) at each time step (see Fig. 2(b)(c)):

$$X^{\mathrm{COM}}(t) = \frac{\int H(x,t)x dx}{\int H(x,t)dx}$$
$$Z^{\mathrm{COM}}(t) = \frac{\int \frac{1}{2}H(x,t)^2 dx}{\int H(x,t)dx} \tag{2}$$

The time derivatives of these quantities yield the bulk horizontal and vertical velocities, $V_x^{\mathrm{COM}}(t)$ and $V_z^{\mathrm{COM}}(t)$. The total bulk velocity is:

$$V_{\mathrm{tot}}(t) = \sqrt{\left(V_x^{\mathrm{COM}}(t)\right)^2 + \left(V_z^{\mathrm{COM}}(t)\right)^2} \tag{3}$$

The temporal evolution of the gravitational potential energy of the granular material is estimated as:

$$E_p(t) = \frac{1}{2}\rho_s \phi_i g^* W \int H(x,t)^2 dx \tag{4}$$

where ϕ_i is solid fraction of the initial granular column, $g^* = g(\rho_s - \rho_w)/\rho_s$ is the effective gravitational acceleration. The corresponding kinetic energy of the bulk motion is given as:

$$E_k(t) = \frac{1}{2}M \cdot \left(V_{\mathrm{tot}}(t)\right)^2 \tag{5}$$

where $M = \rho_s \varphi_i W H_0$ is the total mass of the granular column. The total energy loss over time is thus calculated as:

$$E_{\mathrm{tot}}(t) = E_p(0) - (E_p(t) + E_k(t)) \tag{6}$$

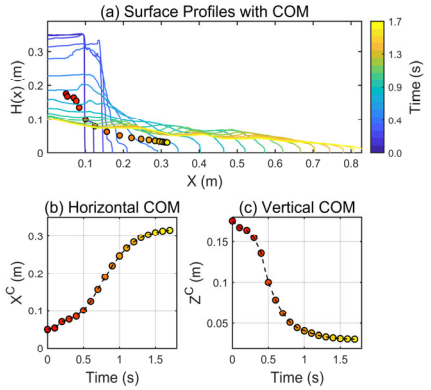

Figure 2. (a) The temporal evolution of the top surface profile H (x, t); (b) and (c) Time evolution of the horizontal and vertical position of the COM, respectively.

2.3.2 *Seismic Parameters*

To quantify the dynamics of submarine granular flows through their seismic emissions, we extract a series of time- and frequency-domain parameters from the vertical ground motion signal $A_Z(t)$ measured by the accelerometers attached beneath the plate. The vertical velocity of the plate surface, denoted $U_Z(t)$, is obtained by integration of $A_Z(t)$ over time.

In the time domain, we compute the signal envelope $Env(t)$ and its maximum value A_{max} via the Hilbert transform of $A_Z(t)$. The signal duration ts is defined as the time interval during which $Env(t)$ exceeds twice the mean absolute noise level. To improve accuracy, low-amplitude signal fluctuations caused by water wave persisting after the main energy release are considered background noise and excluded from ts.

We then perform Fourier transformation on the seismic signals $A_Z(t)$ to analyze their spectra and amplitude spectra $|A_Z(f)|$. In this frequency domain, we characterize the amplitude spectrum with its centroid frequency f_{cen} defined as:

$$f_{cen} = \frac{\int_0^{+\infty} |A_Z(f)| f df}{\int_0^{+\infty} |A_Z(f)| df} \tag{7}$$

which averages the contributions of all impacting particles in the granular flow. The dominant frequency f_{dom} is defined as the peak of the amplitude spectrum, representing the most energetic component of the signal.

Seismic energy provides a proxy for kinetic energy dissipation during granular collapse. In our setup, particle impacts on the basal plate generate elastic waves that propagate and reflect within the plate. Following the diffuse method (Farin et al., 2016; Farin et al., 2019a), we assume that the seismic energy induced by granular impacts is rapidly distributed throughout the plate due to multiple internal reflections. This spatial homogenization allows the use of a single measurement location to represent the overall seismic energy emitted during the flow. The cumulative seismic energy is calculated as:

$$W_{el}(t) = M_p \gamma v_g \int_0^{+\infty} \overline{U_Z(t)}^2 \, dt \tag{8}$$

where M_p is the mass of the PMMA basal plate, $\gamma \approx 3\ m^{-1}$ is the average viscoelastic attenuation coefficient, and $v_g \approx 1200$ m/s is the group velocity of $A0$ Lamb waves. The values of γ and v_g are adopted from Bachelet et al. (2023), who used PMMA plates of similar thickness (1 cm).

3 INTERPRETATION OF RESULTS

3.1 *Dynamics of Immersed Granular Collapses*

3.1.1 *Characteristics of Runout Distance*

After the gate is removed, the granular column begins to collapse, releasing a wedge-shaped mass of grains that initially moves downward before spreading horizontally along the base. The final deposits of submarine collapses exhibit a wavy morphology (see Figure 2(a)), arising from intense fluid–grain coupling near the free surface that enhances local suspension, turbulence generation, and non-uniform settling. At the free surface, relative motion between grains and fluid induces turbulence, vortex shedding, and pressure fluctuations (Gimbert et al., 2014; Polanía et al., 2024), which modulate local deposition rates and produce the observed undulating patterns.

Figure 3(a) shows the temporal evolution of the $\tilde{L}$. Three distinct phases are identified: an initial acceleration phase, a steady propagation stage, and a final deceleration stage. The front initially accelerates from rest, then enters a quasi-steady regime characterized by an approximately constant velocity, before undergoing gradual deceleration until reaching the final runout distance L_f. This general behaviour is consistent across various initial column heights. To quantify the steady propagation stage, the front velocity U is computed. Fig. 3(b) shows the resulting steady velocity U as a function of the initial column height H_0. The steady velocity U increases with H_0, indicating that taller columns generate greater front velocities during the steady propagation stage. The measured velocities scale with the theoretical free-fall velocity $U_{ff} = \sqrt{2g^* H_0}$, where $g^* = g(\rho_s - \rho_w)/\rho_s$ accounts for buoyancy effects. A good agreement is observed when U_{ff} is scaled by a factor of 0.25. This value is consistent with previous research for granular column collapses in the inertial regime, such as a scaling factor of ~0.28 (Bougouin & Lacaze, 2018, Polanía et al., 2024), highlighting the significant influence of interstitial fluid resistance and fluid–particle interactions in submerged environments.

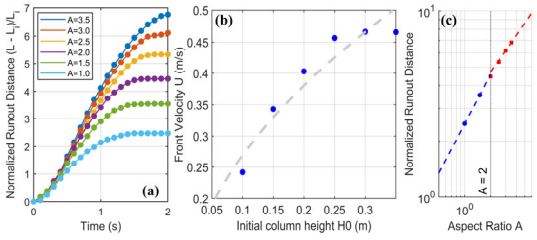

Figure 3. (a) The $\tilde{L}$ evolution; (b) The U during steady propagation versus H_0; (c) The normalized final runout distance as a function of aspect ratio A. The dashed lines indicate the fitted power-law functions.

The mobility of granular column, expressed as the normalized runout distance increases with the aspect ratio A and follows a power-law relationship of the form $\tilde{L} = aA^b$ as previously reported by Lube et al. (2004), Zenit (2005). As shown in Figure 3(c), we obtained best-fit parameters (a, b) = (2.48, 0.88) for short columns (A<2) and (a, b) = (2.98, 0.66) for tall columns (A≥2), which are close to the values reported by and Polanía et al. (2024).

3.1.2 *Basal Normal Stress and Pore Pressure Evolution*

Figure 4(a) shows the temporal evolution of the corrected effective normal stress at PPT_L2 during collapse experiments with varying initial aspect ratios A. The effective stress was obtained by subtracting the corrected pore pressure (removing wave-induced components via PPT_sw) from the total stress recorded at the corresponding load cell (see Figure 4(b)). Results show that columns with larger A generate higher peak effective stresses and more pronounced stress fluctuations, reflecting stronger dynamic interactions between the collapsing granular mass and the base. Additionally, the duration of elevated effective stress is slightly extended for taller columns, indicating prolonged momentum transfer to the basal interface. These findings suggest that the initial geometry significantly influences the basal loading characteristics and may affect the erosion or deformation potential of the underlying substrate during collapse.

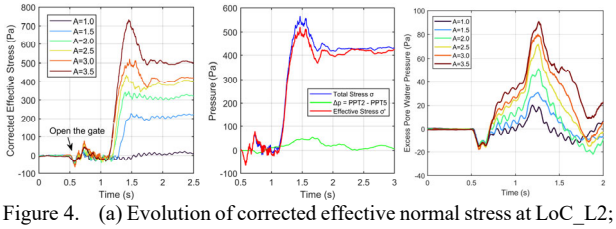

Figure 4. (a) Evolution of corrected effective normal stress at LoC_L2; (b) Correction of surface wave-induced pressure; (c) Temporal evolution of pore water pressure at PPT_L2.

Pore water pressure reflects the pressure exerted by the fluid within the pore spaces of the granular material and plays a crucial role in controlling the effective stress and mechanical behavior of underwater granular flows. As shown in Figure 4(c), pore water pressure rises sharply following collapse initiation, with peak magnitudes increasing as A grows larger. Larger A correspond to taller columns, which induce stronger fluid displacement and compaction effects, leading to higher and more prolonged pore pressure peaks. After reaching the peak, pore pressure gradually dissipates as the flow stabilizes.

3.1.3 *Energy Conversion*

Figure 5 illustrates the temporal evolution of the kinetic energy $E_{\mathrm{k}}(t)$, potential energy $E_{\mathrm{p}}(t)$, and total dissipated energy $E_{\mathrm{tot}}(t)$ during underwater granular column collapse experiments for a range of initial aspect ratios A. As the collapse initiates, gravitational potential energy is rapidly converted into kinetic energy. However, this kinetic energy is short-lived and diminishes quickly due to energy dissipation from viscous drag, inter-particle collisions, and fluid-particle interactions. The data indicate that the proportion of potential energy converted into kinetic energy and subsequently dissipated increases with aspect ratio, highlighting the strong dependence of energy partitioning on initial geometry.

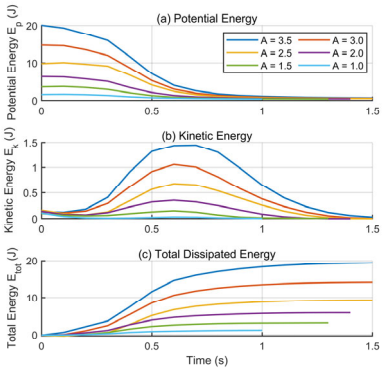

Figure 5. Temporal evolution of the (a) potential energy, (b) kinetic energy, and (c) total dissipated energy with a range of initial aspect ratios A.

3.2 *Dimensional Analysis of Surge Front Stress*

The surge front, as the leading edge of the flow, plays a crucial role by driving bed erosion and generating peak impact forces, thus strongly influencing flow behavior (Choi & Song, 2023; Ng et al., 2014). In this study, we define that a particle is considered as being part of the surge front if its horizontal position x satisfies $x>L-0.5L_0$ (see Figure 6(a)). We interpret the surge front properties and internal stress characteristics at five characteristic time instances, corresponding to the moments when the leading edge of the granular flow reaches normalized runout distances $\tilde{L}$ of 1.5, 2.0, 2.5, 3.0, and 3.5.

As shown in Figure 6(b), based on PIV analysis, the surge front velocity at each time instance is calculated as the average horizontal (x direction) velocity of all particles located within the defined surge front region. As illustrated in Figure 5(b), the overall kinetic energy of the system increases during the initial acceleration phase and then gradually decreases. Therefore, for each of the five front positions, the maximum surge front velocity V_{ft} can be extracted, and the corresponding average surge front thickness H_{ft} is also determined by calculating the average vertical height of particles within the surge front. The deceleration and eventual stoppage of the surge front are governed by the balance between driving and resisting stresses. These resisting forces arise from grain–grain collisions, interparticle friction, and viscous drag exerted by the surrounding fluid. To interpret the stress regime governing the surge front, we employ dimensionless numbers that quantify the relative importance of different stresses. The Savage number N_{S} (Savage & Hutter, 1989) characterizes the ratio of collisional to frictional stresses, with N_{S} >0.1 indicating a dominance of collisional interactions. The Bagnold number N_{B} (Bagnold, 1954) compares collisional grain stresses with viscous fluid stresses, where N_{B}>200 implies that collisional effects prevail over viscous dissipation.

$$N_B = \frac{\overline{\phi_{\mathrm{ft}}}\rho_{\mathrm{s}} d_{\mathrm{p}}^2 \dot{\gamma}}{(1-\overline{\phi_{\mathrm{ft}}})\mu_{\mathrm{f}}} \tag{9}$$

$$N_S = \frac{\rho_{\mathrm{s}} d_{\mathrm{p}}^2 \dot{\gamma}^2}{(\rho_{\mathrm{s}}-\rho_{\mathrm{w}})gH_{\mathrm{ft}}tan\theta} \tag{10}$$

where $\overline{\phi_{\mathrm{ft}}}$ is the estimated front solid volume fraction, $\dot{\gamma}$ is the shear rate, and θ is internal friction angle (22°). We focus on the propagation of the surge front, so $\dot{\gamma}$ can be calculated as $V_{\mathrm{ft}}/H_{\mathrm{ft}}$. The front solid volume fraction $\overline{\phi_{\mathrm{ft}}}$ is estimated based on the time-resolved surface profile H (x, t). As shown in Figure 6(c), we find that ϕ_{ft} remains approximately constant at different normalized runout distances. Therefore, the values of $\overline{\phi_{\mathrm{ft}}}$ reported in Table 1 are calculated as the time-averaged solid volume fractions over these five positions.

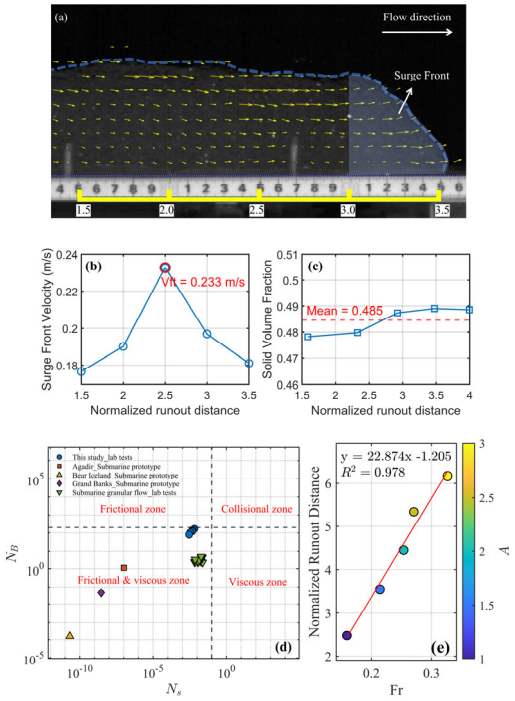

Figure 6. (a) Observed flow front kinematics; (b) Surge front velocity evolution; (c) Solid fraction evolution; (d) Comparison of the lab and field data (data from Choi & Yu, 2023, Elverhoi et al., 2010, Marr et al., 2002, Stevenson et al., 2018, Talling, 2013, Talling et al., 2007); (e) Linear correlation between the $\tilde{L}$ and the Fr.

Figure 6(d) shows a comparison of the grain and fluid stresses between the experimental and field studies. It is observed that submarine flows are predominantly governed by frictional and viscous shear stresses, and the particle collision is not the major source of resistance. This trend is consistent across both field measurements and scaled laboratory experiments, reflecting the damping influence of the interstitial fluid on particle collisions. By contrast, subaerial debris flows, and dry granular avalanches exhibit stress regimes primarily controlled by collisional and frictional interactions, because the absence of a viscous interstitial fluid allows particles to collide directly with high

relative velocities, making collisions and friction the main mechanisms of momentum transfer (Choi et al., 2020; Choi & Song, 2023; Choi & Yu, 2023).

Beyond the mesoscopic grain–fluid stress balance, previous studies have shown that hydroplaning can act as an additional mechanism reducing basal resistance and enhancing mobility in submarine flows. The densimetric Froude number *Fr* is commonly used to evaluate the necessary condition for hydroplaning in submarine granular flows.

$$F_r = \frac{V_{ft}}{\sqrt{\left(\frac{\rho_s}{\rho_w} - 1\right) g H_{ft}}} \tag{11}$$

Figure 6(e) shows a clear linear correlation between the normalized runout distance and *Fr*. Remarkably, this relationship appears to be independent of column size or aspect ratio, yielding a coefficient of determination as high as 0.978. Similar trends were also observed by Yang et al. (2020), reinforcing the link between hydroplaning and enhanced runout in submarine granular flows. This observation implies that the *Fr* can serve as a reliable predictor of runout behavior, regardless of initial granular mass geometry. It can be used to estimate submarine flow mobility, aiding hazard assessment and the design of coastal and offshore structures.

3.3 *Effects of Aspect Ratio on Seismic Signal Characteristics*

As seen in Figure 7(a), larger *A* values produce stronger and longer-lasting seismic envelope amplitudes, reflecting more intense basal force fluctuations and prolonged dynamic interaction between the granular mass and the base. Figures 7(b) to 7(d) shows the dependence of key seismic parameters (dominant frequency, centroid frequency, signal duration) on the initial aspect ratio. The centroid frequency content and duration time of signals increase with *A*. In contrast, the dominant frequency corresponding to the peak frequency in the power spectrum, shows a weak and inconsistent dependence on *A*. While a slight upward trend is observed, the dominant frequency is relatively stable across different aspect ratios, implying that the peak vibration frequency is governed by more complex factors such as base rigidity and material properties, rather than aspect ratio alone.

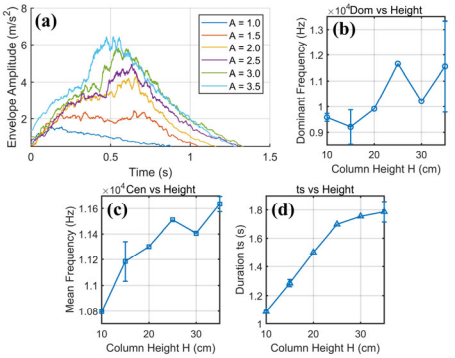

Figure 7. (a) Envelope of seismic signals; (b), (c) and (d) Variation of dominant frequency, centroid frequency, signal duration *ts* with different initial height.

Figures 8(a) and 8(b) show how the cumulative seismic energy $W_{el}(t)$, evolves with time and different initial aspect ratios. The seismic energy $W_{el}(t)$ ($W_{el} \sim A^{1.42}$) increases with aspect ratio *A*, indicating that taller columns release more energy into the ground during collapse. Furthermore, higher-*A* cases also show longer-lasting energy increase, indicating the seismic energy accumulates progressively as the granular flow interacts with the base over an extended time.

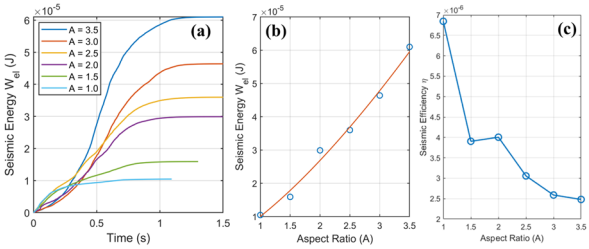

Figure 8. (a) Temporal evolution of the W_{el}; (b) The W_{el} as a function of *A* ($W_{el} \sim A^{1.42}$); (c) Relationship between *A* and seismic efficiency.

3.4 *Correlation Between Dynamic and Seismic Parameters*

To link the dynamic and seismic characteristics of granular flow, the seismic efficiency (i.e., the ratio of radiated seismic energy W_{el} to potential energy lost or total energy lost) is used to quantify how effectively the mechanical energy lost during particle motion is converted into radiated seismic energy that can be measured by sensors (Farin et al., 2019a). A higher seismic efficiency indicates a more effective coupling between mechanical energy and seismic wave generation, while a lower value suggests that most energy is lost through other dissipative processes. In our underwater granular collapse experiments, we observe that the seismic efficiency decreases as the initial aspect ratio *A* of the granular column increases (Figure 8(c)). This trend can be attributed to the distinctive characteristics of submerged granular flows, where fluid–particle interactions and viscous dissipation play significant roles in energy attenuation.

4 CONCLUSIONS

This study investigated the dynamics of submarine granular column collapses and seismic emission with different initial aspect ratios. The results reveal several key findings: (1) Tall columns produce long runout distances, stronger basal stresses, and more energetic seismic emissions, with seismic signals showing increased mean frequency and duration as aspect ratio increases. (2) Dimensional analysis reveals that submarine granular flows are predominantly governed by frictional and viscous stresses, with a linear link between normalized runout and the densimetric Froude number. *Fr* can be used to estimate flow mobility, regardless of initial granular mass geometry. (3) Although columns with higher aspect ratios release more mechanical energy overall, their seismic efficiency decreases due to increased energy dissipation caused by stronger fluid–particle interactions.

5 ACKNOWLEDGEMENTS

The work described in this paper was fully supported by a grant from the Research Grants Council of the Hong Kong Special Administrative Region, China (Project No. C7085-24G_ CRF 2024/25).

6 REFERENCES

Arran, M. I., Mangeney, A., De Rosny, J., & Toussaint, R. (2024). Simulated slidequakes: Insights from DEM simulations into the high-frequency seismic signal generated by geophysical granular flows. *Journal of Geophysical Research: Earth Surface*, *129*(8), e2023JF007455.

Bachelet, V., Mangeney, A., Toussaint, R., de Rosny, J., Arran, M. I., Farin, M., & Hibert, C. (2023). Acoustic emissions of nearly steady and uniform granular flows: A proxy for flow dynamics and velocity fluctuations. *Journal of Geophysical Research: Earth Surface*, *128*(4), e2022JF006990.

Bagnold, R. A. (1954). Experiments on a gravity-free dispersion of large solid spheres in a Newtonian fluid under shear. *Proceedings of the Royal Society of London. Series A. Mathematical and Physical Sciences*, *225*(1160), 49-63.

Baker, M. L., Talling, P. J., Burnett, R., Pope, E. L., Ruffell, S. C., Urlaub, M., ... & Parsons, D. R. (2024). Seabed seismographs reveal duration and structure of longest runout sediment flows on Earth. *Geophysical Research Letters*, *51*(23), e2024GL111078.

Bougouin, A., & Lacaze, L. (2018). Granular collapse in a fluid: Different flow regimes for an initially dense-packing. *Physical Review Fluids*, *3*(6), 064305.

Clare, M. A., Lintern, G., Pope, E., Baker, M., Ruffell, S., Zulkifli, M. Z., ... & Talling, P. J. (2024). Seismic and acoustic monitoring of submarine landslides: Ongoing challenges, recent successes, and future opportunities. *Noisy Oceans: Monitoring Seismic and Acoustic Signals in the Marine Environment*, 59-82.

Choi, C. E., Ng, C. W. W., Liu, H., & Wang, Y. (2020). Interaction between dry granular flow and rigid barrier with basal clearance: analytical and physical modelling. *Canadian Geotechnical Journal*, *57*(2), 236-245.

Choi, C. E., & Song, P. (2023). New unsaturated erosion model for landslide: Effects of flow particle size and debunking the importance of frictional stress. *Engineering Geology*, *315*, 107024.

Choi, C. E., & Yu, J. (2023). Mesoscopic dimensional analysis of submarine debris flows: implications for physical modelling. *Granular Matter*, *25*(1), 14.

Courrech du Pont, S., Gondret, P., Perrin, B., & Rabaud, M. (2003). Granular avalanches in fluids. *Physical review letters*, *90*(4), 044301.

Cook, K. L., & Dietze, M. (2022). Seismic advances in process geomorphology. *Annual Review of Earth and Planetary Sciences*, *50*(1), 183-204.

De Lange, S. I., Santa, N., Pudasaini, S. P., Kleinhans, M. G., & de Haas, T. (2020). Debris-flow generated tsunamis and their dependence on debris-flow dynamics. *Coastal Engineering*, *157*, 103623.

Du, J., Yu, J., & Choi, C. E. (2023). Effects of bed permeability and roughness on the mobility of submarine debris flows: experimental insights. *Landslides*, *20*(3), 497-510.

Duncan, A. J., Gavrilov, A. N., McCauley, R. D., Parnum, I. M., & Collis, J. M. (2013). Characteristics of sound propagation in shallow water over an elastic seabed with a thin cap-rock layer. *The Journal of the Acoustical Society of America*, *134*(1), 207-215.

Elverhoi, A., Breien, H., De Blasio, F. V., Harbitz, C. B., & Pagliardi, M. (2010). Submarine landslides and the importance of the initial sediment composition for run-out length and final deposit. *Ocean Dynamics*, *60*(4), 1027-1046.

Farin, M., Mangeney, A., De Rosny, J., Toussaint, R., Sainte-Marie, J., & Shapiro, N. M. (2016). Experimental validation of theoretical methods to estimate the energy radiated by elastic waves during an impact. *Journal of Sound and Vibration*, *362*, 176-202.

Farin, M., Mangeney, A., De Rosny, J., Toussaint, R., & Trinh, P. T. (2019a). Relations between the characteristics of granular column collapses and resultant high-frequency seismic signals. *Journal of Geophysical Research: Earth Surface*, *124*(12), 2987-3021.

Farin, M., Tsai, V. C., Lamb, M. P., & Allstadt, K. E. (2019b). A physical model of the high-frequency seismic signal generated by debris flows. *Earth Surface Processes and Landforms*, *44*(13), 2529-2543.

Gimbert, F., Tsai, V. C., & Lamb, M. P. (2014). A physical model for seismic noise generation by turbulent flow in rivers. *Journal of Geophysical Research: Earth Surface*, *119*(10), 2209-2238.

Hampton, M. A., Lee, H. J., & Locat, J. (1996). Submarine landslides. *Reviews of geophysics*, *34*(1), 33-59.

Ilstad, T., Marr, J. G., Elverhøi, A., & Harbitz, C. B. (2004). Laboratory studies of subaqueous debris flows by measurements of pore-fluid pressure and total stress. *Marine Geology*, *213*(1-4), 403-414.

Jiang, Y., Zhao, Y., Choi, C. E., & Choo, J. (2022). Hybrid continuum–discrete simulation of granular impact dynamics. *Acta Geotechnica*, *17*(12), 5597-5612.

Jop, P., Forterre, Y., & Pouliquen, O. (2005). Crucial role of sidewalls in granular surface flows: consequences for the rheology. *Journal of fluid mechanics*, *541*, 167-192.

Kunath, P., Talling, P. J., Lange, D., Chi, W. C., Baker, M. L., Urlaub, M., & Berndt, C. (2025). Ocean-bottom seismometers reveal surge dynamics in Earth's longest-runout sediment flows. *Communications Earth & Environment*, *6*(1), 147.

Lube, G., Huppert, H. E., Sparks, R. S. J., & Hallworth, M. A. (2004). Axisymmetric collapses of granular columns. *Journal of Fluid Mechanics*, *508*, 175-199.

Marr, J. G., Elverhøi, A., Harbitz, C., Imran, J., & Harff, P. (2002). Numerical simulation of mud-rich subaqueous debris flows on the glacially active margins of the Svalbard–Barents Sea. Marine Geology, 188(3-4), 351-364.

Ng, C. W. W., Choi, C. E., Goodwin, S. R., & Cheung, W. W. (2017). Interaction between dry granular flow and deflectors. *Landslides*, *14*(4), 1375-1387.

Ng, C. W. W., Choi, C. E., Kwan, J. S. H., Koo, R. C. H., Shiu, H. Y. K., & Ho, K. K. S. (2014). Effects of baffle transverse blockage on landslide debris impedance. *Procedia Earth and Planetary Science*, *9*, 3-13.

Ng, C. W. W., Choi, C. E., & Law, R. P. H. (2013). Longitudinal spreading of granular flow in trapezoidal channels. *Geomorphology*, *194*, 84-93.

Paull, C. K., Talling, P. J., Maier, K. L., Parsons, D., Xu, J., Caress, D. W., ... & Cartigny, M. J. (2018). Powerful turbidity currents driven by dense basal layers. *Nature communications*, *9*(1), 4114.

Polanía, O., Estrada, N., Azéma, E., Renouf, M., & Cabrera, M. (2024). Polydispersity effect on dry and immersed granular collapses: an experimental study. *Journal of Fluid Mechanics*, *983*, A40.

Sarlin, W., Morize, C., Sauret, A., & Gondret, P. (2021). Collapse dynamics of dry granular columns: From free-fall to quasistatic flow. *Physical Review E*, *104*(6), 064904.

Savage, S. B., & Hutter, K. (1989). The motion of a finite mass of granular material down a rough incline. *Journal of fluid mechanics*, *199*, 177-215.

Stamhuis, E., & Thielicke, W. (2014). PIVlab–towards user-friendly, affordable and accurate digital particle image velocimetry in MATLAB. *Journal of open research software*, *2*(1), 30.

Stevenson, C. J., Feldens, P., Georgiopoulou, A., Schönke, M., Krastel, S., Piper, D. J., ... & Mosher, D. (2018). Reconstructing the sediment concentration of a giant submarine gravity flow. *Nature communications*, *9*(1), 2616.

Su, Y., & Choi, C. E. (2021). Effects of particle shape on the cushioning mechanics of rock-filled gabions. *Acta Geotechnica*, *16*(4), 1043-1052.

Talling, P. J. (2013). Hybrid submarine flows comprising turbidity current and cohesive debris flow: Deposits, theoretical and experimental analyses, and generalized models. *Geosphere*, *9*(3), 460-488.

Talling, P. J., Baker, M. L., Pope, E. L., Ruffell, S. C., Jacinto, R. S., Heijnen, M. S., ... & Hilton, R. J. (2022). Longest sediment flows yet measured show how major rivers connect efficiently to deep sea. *Nature communications*, *13*(1), 4193.

Talling, P. J., Cartigny, M. J., Pope, E., Baker, M., Clare, M. A., Heijnen, M., ... & Maier, K. L. (2023). Detailed monitoring reveals the nature of submarine turbidity currents. Nature Reviews Earth & Environment, 4(9), 642-658.

Talling, P. J., Wynn, R. B., Masson, D. G., Frenz, M., Cronin, B. T., Schiebel, R., ... & Amy, L. A. (2007). Onset of submarine debris flow deposition far from original giant landslide. *Nature*, *450*(7169), 541-544.

Tsai, V. C., Minchew, B., Lamb, M. P., & Ampuero, J. P. (2012). A physical model for seismic noise generation from sediment transport in rivers. *Geophysical Research Letters*, *39*(2).

Walder, J. S., Watts, P., Sorensen, O. E., & Janssen, K. (2003). Tsunamis generated by subaerial mass flows. *Journal of Geophysical Research: Solid Earth*, *108*(B5).

Yang, G. C., Jing, L., Kwok, C. Y., & Sobral, Y. D. (2020). Pore-scale simulation of immersed granular collapse: implications to submarine landslides. *Journal of Geophysical Research: Earth Surface*, *125*(1), e2019JF005044.

Zenit, R. (2005). Computer simulations of the collapse of a granular column. *Physics of Fluids*, *17*(3).

Zhang, Z., Walter, F., McArdell, B. W., de Haas, T., Wenner, M., Chmiel, M., & He, S. (2021). Analyzing bulk flow characteristics of debris flows using their high frequency seismic signature. *Journal of Geophysical Research: Solid Earth*, *126*(12), e2021JB022755.